Spin current from sub-terahertz-generated antiferromagnetic magnons

https://doi.org/10.1038/s41586-020-1950-4

Received: 11 January 2019

Accepted: 22 October 2019

Published online: 27 January 2020

Junxue Li[1], C. Blake Wilson[2,3], Ran Cheng[1,4], Mark Lohmann[1], Marzieh Kavand[2,3], Wei Yuan[1], Mohammed Aldosary[1], Nikolay Agladze[2,3], Peng Wei[1], Mark S. Sherwin[2,3] & Jing Shi[1]*

Spin dynamics in antiferromagnets has much shorter timescales than in ferromagnets, offering attractive properties for potential applications in ultrafast devices[1–3]. However, spin-current generation via antiferromagnetic resonance and simultaneous electrical detection by the inverse spin Hall effect in heavy metals have not yet been explicitly demonstrated[4–6]. Here we report sub-terahertz spin pumping in heterostructures of a uniaxial antiferromagnetic Cr_2O_3 crystal and a heavy metal (Pt or Ta in its β phase). At 0.240 terahertz, the antiferromagnetic resonance in Cr_2O_3 occurs at about 2.7 tesla, which excites only right-handed magnons. In the spin-canting state, another resonance occurs at 10.5 tesla from the precession of induced magnetic moments. Both resonances generate pure spin currents in the heterostructures, which are detected by the heavy metal as peaks or dips in the open-circuit voltage. The pure-spin-current nature of the electrically detected signals is unambiguously confirmed by the reversal of the voltage polarity observed under two conditions: when switching the detector metal from Pt to Ta, reversing the sign of the spin Hall angle[7–9], and when flipping the magnetic-field direction, reversing the magnon chirality[4,5]. The temperature dependence of the electrical signals at both resonances suggests that the spin current contains both coherent and incoherent magnon contributions, which is further confirmed by measurements of the spin Seebeck effect and is well described by a phenomenological theory. These findings reveal the unique characteristics of magnon excitations in antiferromagnets and their distinctive roles in spin–charge conversion in the high-frequency regime.

Owing to their terahertz spin dynamics and absence of net magnetization, antiferromagnetic (AFM) materials offer unique advantages for ultrafast and robust spin-based nanoscale device applications[10–16]. A prerequisite for practical AFM-based spintronics is the generation and electrical detection of pure spin currents. Cheng et al.[4] and Johansen et al.[5] proposed to generate coherent magnon spin currents by inducing uniform spin precession at the antiferromagnetic resonance (AFMR) with terahertz radiation. This mechanism works in the collinear AFM phase at arbitrary magnetic fields (even zero field) below the spin-flop transition. Ross et al.[6] detected d.c. voltages at the AFMR in MnF_2, but concluded that the main d.c. voltage was from the microwave rectification effect or heating-related thermoelectric electromotive force (EMF). Clear AFM spin pumping has yet to be experimentally established. Here we demonstrate the generation and simultaneous electrical detection of pure spin currents in a uniaxial AFM material, Cr_2O_3. The former is accomplished by driving the AFM spin precession into resonance using linearly polarized sub-terahertz radiation. Through the inverse spin Hall effect (ISHE), the resonantly generated spin current is converted into a d.c. voltage.

Cr_2O_3 is a uniaxial AFM insulator with the easy axis along the *c* axis of the hexagonal lattice[17] (Extended Data Fig. 1). Because of its relatively simple spin structure and accessible AFMR frequency (about 0.165 THz at 0 K) and spin-flop field (6.0 T at 0 K)[18,19], Cr_2O_3 is chosen for this study. As shown in Fig. 1a, 0.240-THz continuous microwaves are generated by a solid-state source and propagate into a corrugated waveguide at the centre of a 12.5-T superconducting magnet. The Cr_2O_3 $(10\bar{1}0)$ slab is mounted on a piece of sapphire secured on a Teflon stage located at the exit of the waveguide. Figure 1b depicts the sample structure and measurement geometry. The sample is oriented with the *c* axis parallel to both the d.c. magnetic field, $\mathbf{H}_0$, and the microwave propagation direction, $\mathbf{k}$. The microwave magnetic-field component $\mathbf{h}$ is kept in the sample plane and perpendicular to the *c* axis of Cr_2O_3. Similarly to conventional ferromagnetic spin pumping, the AFM spins in Cr_2O_3 are driven into resonance at a fixed, but much higher, microwave frequency by sweeping the d.c. magnetic field. A pure spin current is then injected into the adjacent heavy-metal layer, which in turn produces a charge current in Pt, Ta or the Pt–Ta hybrid channel (Methods) through the ISHE and results in an open-circuit d.c. voltage, V_{ISHE}. Microwaves reflected by the sample are detected by a superheterodyne receiver and recorded as electron magnetic resonance (EMR) signals (Methods)[20,21]. Both EMR and electrical voltage signals are simultaneously measured using the standard lock-in technique.

[1]Department of Physics and Astronomy, University of California, Riverside, CA, USA. [2]Physics Department, University of California, Santa Barbara, CA, USA. [3]Institute for Terahertz Science and Technology, University of California, Santa Barbara, CA, USA. [4]Department of Electrical and Computer Engineering, University of California, Riverside, CA, USA. *e-mail: jing.shi@ucr.edu

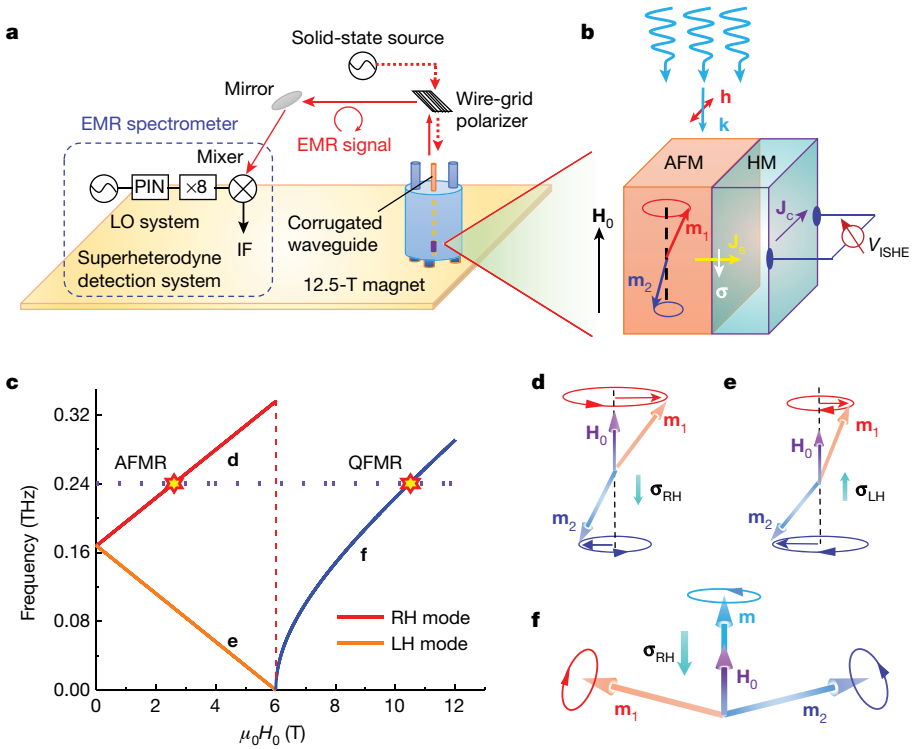

Fig. 1 | AFM spin dynamics and pure spin current in an AFM/heavy-metal heterostructure. a, Continuous-wave (CW) EMR system (see Methods). A 0.240-THz CW is generated by a solid-state source and polarized by a wire-grid polarizer before entering the waveguide. The sample is loaded into a continuous-flow cryostat mounted in the room-temperature bore of the magnet. CW EMR measurements are carried out using source-intensity modulation with a frequency of 13.037 Hz. The reflected CWs are measured by a superheterodyne detection system using a local oscillator (LO) and a Schottky subharmonic mixer to mix the 0.240-THz signal to 10 GHz. Then, a home-built intermediate-frequency (IF) stage amplifies and mixes this signal down to baseband. The resulting signal is measured in quadrature with a pair of lock-in amplifiers. PIN, p–i–n switch. **b**, Sample structure and spin-current injection. Two sublattice magnetic moments, $\mathbf{m}_1$ and $\mathbf{m}_2$, are excited into resonance, and the spin current $\mathbf{J}_s$ with spin polarization $\boldsymbol{\sigma}$ generates the charge current $\mathbf{J}_c$ in the heavy-metal (HM) layer. **c**, Magnetic-resonance frequency as a function of the magnetic field $\mu_0 H_0$ (μ_0, magnetic permeability constant) applied along the c axis of Cr_2O_3 at 0 K. The labels **d**, **e** and **f** correspond to the panels at right. **d**–**f**, The eigenmodes of the RH AFMR (**d**), the LH AFMR (**e**), and the QFMR (**f**), as labelled in **c**. $\boldsymbol{\sigma}_{RH}$ and $\boldsymbol{\sigma}_{LH}$ are the spin polarizations associated with RH and LH chirality, respectively.

Figure 1c summarizes the magnetic resonance frequency as a function of $\mathbf{H}_0$ when the magnetic field is applied along the c axis of Cr_2O_3. Below the spin-flop field of 6.0 T, there are two distinct branches corresponding to the two eigenmodes of the AFM spin-wave excitations or magnons, namely, right-hand (RH) and left-hand (LH) spin precessions with opposite chiralities[14,18,19]. At $\mathbf{H}_0 = 0$, these two modes are degenerate at $\omega_m/(2\pi) = 0.165$ THz, as shown in Fig. 1d, e (ω_m is the magnon angular frequency at zero magnetic field). This is fundamentally different from ferromagnetic materials, in which the sole magnon mode is RH. Because these two modes carry equal but opposite angular momenta, $\pm\hbar$ ($\hbar$, reduced Planck constant; ref. [14]), the net spin angular momentum is zero if they are equally populated. When $\mathbf{H}_0$ is applied along the c axis of Cr_2O_3, the degeneracy between RH and LH modes is lifted, and the frequencies of the two branches are given by[19] $\omega/\gamma = \sqrt{2H_E H_A + (H_0\alpha/2)^2} \pm H_0(1-\alpha/2)$, where $\gamma = 28$ GHz T^{-1} is the gyromagnetic ratio, H_E and H_A are effective fields of the inter-sublattice exchange interaction and the easy-axis anisotropy, $\alpha = \chi_\parallel/\chi_\perp$ is the ratio of the magnetic susceptibilities in the parallel and perpendicular directions, and the + (−) sign refers to the RH (LH) mode. At low temperatures, $\alpha \approx 0$ and $\omega/\gamma = \sqrt{2H_E H_A} \pm H_0$, which is represented by the two straight lines in Fig. 1c. In our experiments, the microwaves are linearly polarized, and the frequency is held at 0.240 THz (horizontal dashed line) while $\mathbf{H}_0$ is swept; therefore, only the RH mode can be excited when the upper branch intercepts the horizontal dashed line. For Cr_2O_3, the low-temperature resonance field of the RH mode is estimated to be about 2.7 T, which is confirmed by our EMR experiment (Supplementary Information Note I).

As the $\mathbf{H}_0$ strength reaches the spin-flop field, spins in both sublattices switch abruptly to align nearly perpendicular to $\mathbf{H}_0$ with a small inclination[22]. We observe an EMR feature at the spin-flop transition (Supplementary Information Note I). A new resonance mode emerges above the spin-flop field, as depicted in Fig. 1f. In this mode, the total magnetic moment $\mathbf{m} = \mathbf{m}_1 + \mathbf{m}_2$ precesses around $\mathbf{H}_0$ with RH chirality[19]. This is essentially equivalent to the ferromagnetic resonance mode in ferromagnets. We call it quasi-ferromagnetic resonance (QFMR) mode to distinguish it from the ferromagnetic resonance mode of the fully spin-aligned state, which could only be accessed at extremely high magnetic fields. The QFMR frequency is given by[19] $\omega/\gamma = \sqrt{H_0^2 - 2H_E H_A}$. For $\omega/(2\pi) = 0.240$ THz, the QFMR is estimated to occur at ~10.5 T in Cr_2O_3 (see Supplementary Information Note I for the EMR signal at the QFMR). By sweeping $\mathbf{H}_0$ up to 12 T, we can excite both the RH AFMR and QFMR modes in Cr_2O_3.

At these resonances, uniformly precessing spins in Cr_2O_3 form a $\mathbf{k} = 0$ magnon reservoir. Similar to ferromagnetic spin pumping, when the magnon reservoir is in contact with a heavy-metal layer such as Pt, a pure spin current flows across the interface via magnon–electron interactions and is consequently converted to an open-circuit d.c. voltage in Pt due to the ISHE. We observed electrical voltage signals at both resonance fields identified by EMR signals. To distinguish the pure-spin-current effect from other spurious effects, we use Pt and Ta as two independent detection channels (Extended Data Fig. 2). Because of the opposite sign in their spin Hall angles[7–9], the same pure spin current must produce voltage signals with opposite polarities in the Pt and Ta

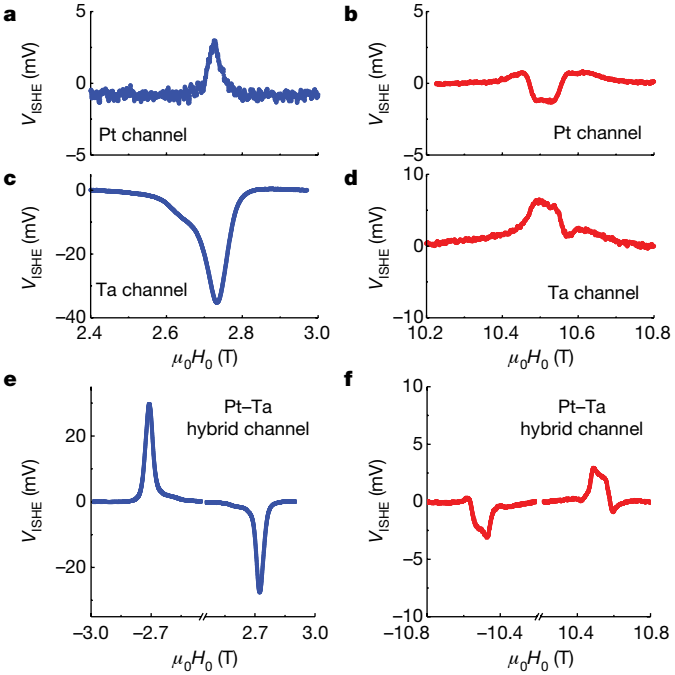

Fig. 2 | ISHE signals at the AFMR and the QFMR. a, **c**, Electrical voltages from the Pt channel (**a**) and the Ta channel (**c**) at the AFMR at 5 K. **b**, **d**, Voltages from the Pt channel (**b**) and the Ta channel (**d**) at the QFMR at 5 K. **e**, **f**, Voltages from the Pt–Ta hybrid channel at the AFMR (**e**) and the QFMR (**f**) for both positive and negative fields at 10 K. The ISHE voltage is dominated by the Ta channel at low temperatures.

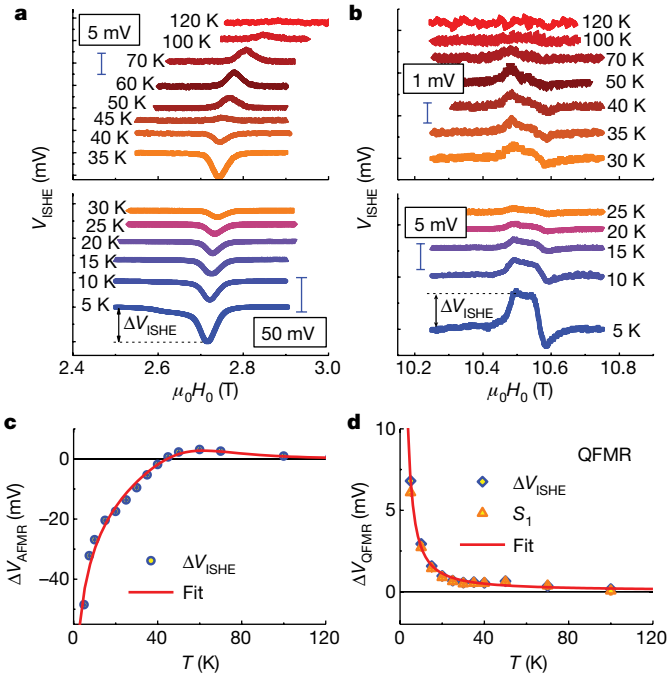

Fig. 3 | Temperature dependence of ISHE signals. a, ISHE voltage signal at the AFMR. **b**, ISHE voltage signal at the QFMR. **c**, Temperature dependence of the ISHE peak height ΔV_{ISHE} (as indicated in **a**) at the AFMR (symbols) and the best fit (line) using equation (S16) in Supplementary Information. **d**, Temperature dependence of the ISHE peak height ΔV_{ISHE} (as indicated in **b**) and of S_1 (symbols): the magnitude of the main symmetric Lorentzian function (see Supplementary Information section III). The red solid line is the best fit using equation (S17) in Supplementary Information. The error bars represent the range of the off-resonance voltage signals. Error bars in **c** and **d** are smaller than the symbols.

channels. On the other hand, any spurious electrical signal generated by microwave rectification or heating-related thermoelectric EMF may maintain the same polarity in Pt and Ta. Indeed, sharp voltage features are unmistakably resolved at 2.7 T in two independent Pt and Ta channels, as shown in Fig. 2a, c. The resonance field corresponds well to the AFMR field identified by EMR. More importantly, the Pt and Ta channels register opposite AFMR voltages at 5 K. At 10.5 T, where the QFMR occurs, the same opposite polarity is observed, as shown in Fig. 2b, d. The opposite voltage polarity between the Pt and Ta channels at both the AFMR and the QFMR is a defining characteristic of the resonantly generated pure spin current. Because the ISHE voltage is proportional to the resistivity of the detecting channel, providing the same spin–charge conversion efficiency, and Ta is much more resistive (by more than a factor of 10) than Pt, we expect a larger voltage response in Ta (Supplementary Information Note II).

After confirming the opposite voltage polarities in the independent Ta-only and Pt-only channels, we wire-bond the neighbouring Pt and Ta strips in series (Extended Data Fig. 2c) to form a single long hybrid channel. All Pt and Ta strips on the chip are connected to further enhance the total voltage signal output. In the following experiments, unless otherwise specified, we adopt this hybrid detector geometry for electrical detection. To corroborate the pure-spin-current nature of the d.c. voltage signals, we reverse the direction of $\mathbf{H}_0$, and therefore the spin polarization of the pumped spin current. We observe a completely inverted voltage signal on the negative-field side (Fig. 2e). The same complete voltage inversion is observed for the QFMR despite the complicated line shape (shown in Fig. 2f). We note that heating-related thermoelectric EMF cannot produce voltage sign reversal when the magnetic field is reversed. Hence, the observation of the two sign reversals leads us to unambiguously conclude that the d.c. voltage in heavy-metal detectors stems exclusively from pure spin current generated by resonant magnon excitations. Furthermore, we confirm that the ISHE voltages have a linear dependence on the microwave power (Extended Data Fig. 3).

A more rigorous examination of the low-temperature behaviours of the AFMR and QFMR shown in Fig. 2 reveals something counterintuitive. With the same detecting heavy metal, the ISHE voltage feature at the AFMR and the main feature at the QFMR have opposite signs, which contradicts the simple picture of coherent spin pumping. As schematically illustrated in Fig.1d, f, the RH AFMR and the QFMR eigenmodes exhibit the same spin polarization; hence, the resulting ISHE voltages should also have the same polarity for a fixed heavy metal. The apparent contradiction implies that coherent spin pumping is not the sole mechanism. To better understand the origin of the sign discrepancy, we perform ISHE voltage measurements over a wide range of temperatures. Figure 3a shows a plot of the ISHE voltage at the AFMR for positive magnetic fields from 5 K to 120 K. The voltage signal is negative at low temperatures and becomes smaller as the temperature is raised. It crosses zero at about 45 K and stays positive at higher temperatures, until it finally diminishes at around 120 K. A similar sign change is also observed for negative magnetic fields (Extended Data Fig. 4). By contrast, the main ISHE peak at the QFMR (Fig. 3b) always stays positive, and decreases monotonically with increasing temperature until it finally vanishes above 100 K. We also confirmed the sign-change pattern of the ISHE signals by comparing the Pt-only and Ta-only channels (Extended Data Fig. 5).

After carefully analysing the line shape of the d.c. voltage signals at the QFMR at all temperatures (Supplementary Information Note III), we plotted the magnitudes of both the AFMR voltage and the main QFMR peak voltage (Fig. 3c, d). The contrast ends at low temperatures. Clearly, the ISHE voltage at both resonances disappears far below the Néel temperature of the Cr_2O_3 crystal (307 K)[18,19]. We note that the EMR signal at the AFMR is still observable up to 288 K (see

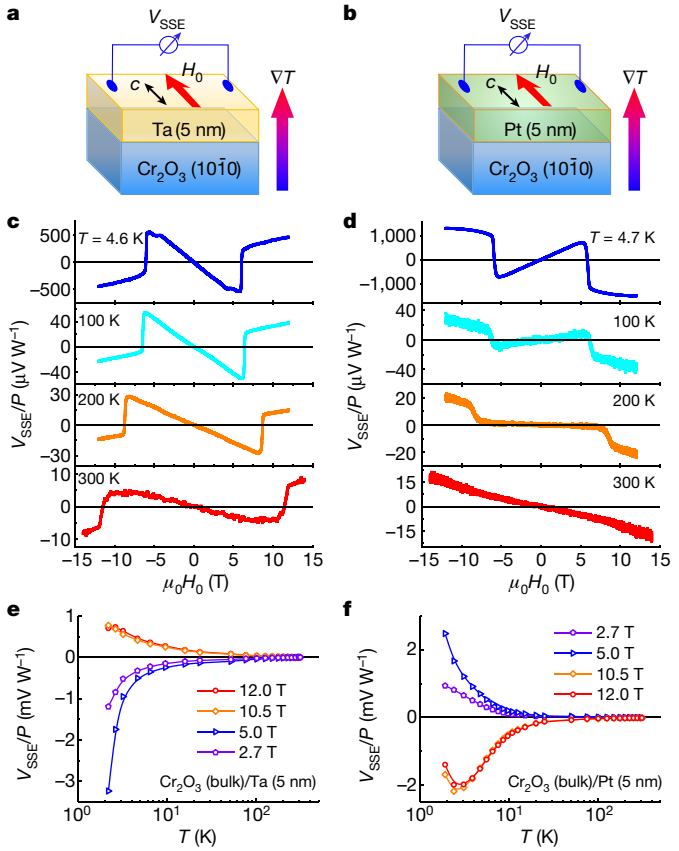

Fig. 4 | SSE from incoherent AFM magnons. a, **b**, SSE measurements in $Cr_2O_3(10\bar{1}0)$/Ta (**a**) and $Cr_2O_3(10\bar{1}0)$/Pt (**b**) heterostructures. The vertical temperature gradient ∇T is generated by an on-chip heater. The magnetic field H_0 is applied in plane and along the *c* axis. **c**, **d**, Field dependence of the SSE signal, normalized to the heating power, at 4.6 K, 100 K, 200 K and 300 K in Cr_2O_3/Ta (**c**) and Cr_2O_3/Pt (**d**) heterostructures. **e**, **f**, Temperature dependence of the SSE signal, normalized to the heating power, under magnetic fields of 2.7 T, 5.0 T, 10.5 T and 12 T in Cr_2O_3/Ta (**e**) and Cr_2O_3/Pt (**f**) heterostructures.

Supplementary Fig. 4), indicating that microwave absorption remains active at least up to room temperature. Because the ISHE voltage depends on the efficiency of the spin–charge conversion, we believe that the quality of the interface may be responsible for the disappearance of the ISHE signals at a lower temperature than the ordering temperature of Cr_2O_3.

The stark contrast between the temperature dependence of the AFMR- and QFMR-induced spin currents indicates that coherent spin pumping alone is inadequate to explain these behaviours. The reasons include: (1) no sign change of the dependence of the spin Hall angle of Pt or Ta on the temperature has ever been reported[7,8]; (2) the absence of sign change for the QFMR further confirms point (1); (3) the spin-polarization direction of the resonant mode is fixed and cannot change with temperature. We propose the following mechanism to explain this unusual temperature dependence. As illustrated in Fig. 1c, whereas the coherently driven AFMR selectively excites the RH mode, thermal excitations of incoherent magnons prefer the LH mode, which has a lower energy. As a result, thermally driven LH magnons compete with coherent RH magnons. When the contribution of the former exceeds that of the latter, it causes a sign change of the total ISHE voltage. Therefore, the sign change strongly suggests rapid thermalization of coherent magnons into incoherent magnons. This process results in an increased effective magnon temperature, which in turn raises the lattice temperature via magnon–phonon scattering. In fact, we observed a temperature rise at the AFMR by monitoring the resistance of the Pt–Ta hybrid channel, which serves as a sensitive thermometer (Supplementary Information Note IV). A similar mechanism has recently been proposed for ferromagnetic spin pumping, which can result in resonance-induced heating[23,24].

The increased incoherent magnon population at the resonances must be accompanied by an additional spin current flowing across the metal–Cr_2O_3 interface, and consequently an additional ISHE voltage of opposite polarity. This process is essentially the same as the spin Seebeck effect (SSE), in which the incoherent magnon diffusion is driven by a temperature gradient. To better understand the incoherent magnon contribution, we performed independent SSE measurements in the same Cr_2O_3/Ta and Cr_2O_3/Pt heterostructures, where coherent magnons were completely eliminated. As illustrated in Fig. 4a, b, we measured the SSE-induced ISHE voltages by sweeping the magnetic field along the *c* axis of the Cr_2O_3 crystal under a vertical temperature gradient generated by a heater on top of the crystal. Figure 4c, d displays the field dependence of the SSE signals in Cr_2O_3/Ta and Cr_2O_3/Pt. First, there is a large SSE signal at low fields. At 6 T—that is, the spin-flop field—the SSE voltage undergoes an abrupt jump and switches sign. The sign switch is exactly what is expected from the magnon energy diagram shown in Fig. 1c. Below the spin-flop transition, the LH-magnon branch has a lower energy, and thus the total thermal magnon population is dominated by LH magnons at low temperatures. Above the spin-flop transition, however, the canted state supports only RH magnons; therefore, the SSE must change sign across the spin-flop transition. The same behaviour was also observed in heterostructures containing epitaxial Cr_2O_3 thin films (Extended Data Fig. 6). The SSE signal in Cr_2O_3/Pt is simply inverted compared to that in Cr_2O_3/Ta for the same reason as in the resonance data. Our SSE signal is quite different from what was reported by Seki et al.[25], which might be caused by the different Cr_2O_3/heavy-metal interface properties (as demonstrated in Extended Data Fig. 7). The temperature dependences of both samples are summarized in Fig. 4e, f for magnetic fields below and above the spin-flop transition and temperatures of up to 310 K. It is interesting to note that the incoherent magnon contribution to the ISHE voltage in Cr_2O_3 alone does not cause any sign change, which is different from the behaviours of some ferrimagnets[26,27] (see discussion in Supplementary Information Note V). As the temperature is decreased, the magnitude of the SSE voltage below the spin-flop field increases precipitously. This trend is the same as that of the AFMR ISHE voltage. Both can be explained by a decreased equilibrium population of RH magnons. At the AFMR, as the temperature is lowered, the increased LH-magnon contribution balances out that of the coherently excited RH magnons at ~45 K. In fact, as the temperature is decreased further, the net LH-magnon population should reach the maximum, and an SSE voltage peak emerges[28]. The peak occurs approximately at temperature T_p when $k_B T_p \approx \hbar\omega_m$, where k_B is the Boltzmann constant. This overall SSE characteristic has been observed in other uniaxial AFM materials, such as MnF_2 and FeF_2[29,30]. Compared to these two materials, Cr_2O_3 has a lower ω_m; hence, the SSE peak should occur at an even lower T_p. We note that the SSE peak was not captured in previous experiments because T_p was outside their temperature range[25], but it appears at ~2.3 K in our experiment, as shown in Fig. 4e, f. In principle, the AFMR ISHE voltage would also show a peak if the temperature range extended below T_p in our resonance experiments. The same proposed coherent-to-incoherent magnon thermalization mechanism should also be applicable for the QFMR, except that both magnons are RH. In the case of the QFMR, the incoherent magnon contribution should be compared with the SSE voltage above the spin-flop transition, as is also shown in Fig. 4e, f.

In Supplementary Information Note VI, we describe the temperature dependence of the ISHE voltages at both the AFMR and the QFMR on the basis of a proposed coherent-to-incoherent thermalization mechanism that converts energy from coherent Néel order precession into phase-random thermal magnons. We capture the thermalization process phenomenologically by a temperature dependent parameter $\eta(T)$, as shown in equations (S8) and (S9) in Supplementary Information. We

further assume that $\eta(T)$ scales as T^a, with the exponent a obtained from fitting the experimental data. The higher the temperature is, the faster incoherent magnons are generated by coherent magnons, which leads to a reduction of coherent spin pumping. On the other hand, the scattering between thermal magnons and phonons also becomes stronger at higher temperatures, which destroys incoherent magnons and eventually transfers energy into phonons. Meanwhile, the net magnon spin-current polarization, characterized by $\xi(T)$ in equation (S15) in Supplementary Information, also decreases with increasing T (Extended Data Fig. 8). The combination of these two mechanisms results in a substantial reduction of incoherent spin current at higher T values. Whereas both coherent and incoherent contributions decay with increasing T, the incoherent contribution varies much faster than the coherent contribution, which explains the crossover in the AFMR ISHE voltage at about 45 K in our experiments. As shown in Fig. 3c, d, our theory fits the experimental data very well.

In the case of the QFMR, coherent and incoherent magnons have the same chirality, so that they generate spin currents with the same polarization; thus, there should be no sign change at any temperature. Similarly to the AFMR case, both contributions decrease with increasing T; thus, the total spin current simply exhibits a monotonic decay with T, which agrees with the experimental data in Fig. 3d. We also notice that the situation of the QFMR is similar to what happens in ferromagnetic spin pumping, where the distinction between coherent and incoherent contributions is quite subtle (even controversial)[23,24]. In this regard, we believe that AFM materials provide a unique playground for studying the interplay between coherent and incoherent magnons.

In summary, we have demonstrated the generation and electrical detection of pure spin currents pumped by resonances in uniaxial AFM Cr_2O_3 using sub-terahertz radiation, and have unequivocally confirmed the ISHE nature of the voltage signals. The intriguing temperature dependences of the ISHE voltages at both the AFMR and the QFMR suggest that coherent and incoherent magnons contribute to the spin current, with the latter dominating at low temperatures. Our experimental findings set the stage for further exploring spin currents in the emerging field of AFM spintronics.

Online content

Any methods, additional references, Nature Research reporting summaries, source data, extended data, supplementary information, acknowledgements, peer review information; details of author contributions and competing interests; and statements of data and code availability are available at https://doi.org/10.1038/s41586-020-1950-4.

1. Gomonay, O., Baltz, V., Brataas, A. & Tserkovnyak, Y. Antiferromagnetic spin textures and dynamics. *Nat. Phys.* **14**, 213–216 (2018).
2. Kampfrath, T. et al. Coherent terahertz control of antiferromagnetic spin waves. *Nat. Photon.* **5**, 31–34 (2011).
3. Tzschaschel, C. et al. Ultrafast optical excitation of coherent magnons in antiferromagnetic NiO. *Phys. Rev. B* **95**, 174407 (2017).
4. Cheng, R., Xiao, J., Niu, Q. & Brataas, A. Spin pumping and spin-transfer torques in antiferromagnets. *Phys. Rev. Lett.* **113**, 057601 (2014).
5. Johansen, Ö. & Brataas, A. Spin pumping and inverse spin Hall voltages from dynamical antiferromagnets. *Phys. Rev. B* **95**, 220408 (2017).
6. Ross, P. et al. Antiferromagentic resonance detected by direct current voltages in MnF_2/Pt bilayers. *J. Appl. Phys.* **118**, 233907 (2015).
7. Hoffmann, A. Spin Hall effects in metals. *IEEE Trans. Magn.* **49**, 5172–5193 (2013).
8. Sinova, J. et al. Spin Hall effects. *Rev. Mod. Phys.* **87**, 1213–1260 (2015).
9. Li, J. et al. Observation of magnon-mediated current drag in Pt/yttrium iron garnet/Pt(Ta) trilayers. *Nat. Commun.* **7**, 10858 (2016).
10. Marti, X. et al. Room-temperature antiferromagnetic memory resistor. *Nat. Mater.* **13**, 367–374 (2014).
11. Wadley, P. et al. Electrical switching of an antiferromagnet. *Science* **351**, 587–590 (2016).
12. Kriegner, D. et al. Multiple-stable anisotropic magnetoresistance memory in antiferromagnetic MnTe. *Nat. Commun.* **7**, 11623 (2016).
13. Kittel, C. Theory of antiferromagnetic resonance. *Phys. Rev.* **82**, 565 (1951).
14. Keffer, F. & Kittel, C. Theory of antiferromagnetic resonance. *Phys. Rev.* **85**, 329–337 (1952).
15. Němec, P., Fiebig, M., Kampfrath, T. & Kimel, A. V. Antiferromagnetic opto-spintronics. *Nat. Phys.* **14**, 229–241 (2018).
16. Baltz, V. et al. Antiferromagnetic spintronics. *Rev. Mod. Phys.* **90**, 015005 (2018).
17. He, X. et al. Robust isothermal electric control of exchange bias at room temperature. *Nat. Mater.* **9**, 579–585 (2010).
18. Dayhoff, E. S. Antiferromagnetic resonance in Cr_2O_3. *Phys. Rev.* **107**, 84 (1957).
19. Foner, S. High-field antiferromagnetic resonance in Cr_2O_3. *Phys. Rev.* **130**, 183–197 (1963).
20. Takahashi, S. et al. Pulsed electron paramagnetic resonance spectroscopy powered by a free-electron laser. *Nature* **489**, 409 (2012).
21. Edwards, D. T., Zhang, Y., Glaser, S. J., Han, S. & Sherwin, M. S. Phase cycling with a 240 GHz, free electron laser-powered electron paramagnetic resonance spectrometer. *Phys. Chem. Chem. Phys.* **15**, 5707 (2013).
22. Bogdanov, A. N., Zhuravlev, A. V. & Robler, U. K. Spin-flop transition in uniaxial antiferromagnets: magnetic phases, reorientation effects, and multidomain states. *Phys. Rev. B* **75**, 094425 (2007).
23. Lin, W. W. & Chien, C. L. Evidence of pure spin current. Preprint at https://arxiv.org/abs/1804.01392 (2018).
24. Chen, Y. S., Lin, J. G., Huang, S. Y. & Chien, C. L. Incoherent spin pumping from YIG single crystals. *Phys. Rev. B* **99**, 220402 (2019).
25. Seki, S. et al. Thermal generation of spin current in an antiferromagnet. *Phys. Rev. Lett.* **115**, 266601 (2015).
26. Geprägs, S. et al. Origin of the spin Seebeck effect in compensated ferrimagnets. *Nat. Commun.* **7**, 10452 (2016).
27. Cramer, J. et al. Magnon mode selective spin transport in compensated ferrimagnets. *Nano Lett.* **17**, 3334 (2017).
28. Rezende, S. M., Rodríguez-Suárez, R. L. & Azevedo, A. Theory of the spin Seebeck effect in antiferromagnets. *Phys. Rev. B* **93**, 014425 (2016).
29. Wu, S. M. et al. Antiferromagnetic spin Seebeck effect. *Phys. Rev. Lett.* **116**, 097204 (2016).
30. Li, J. et al. Spin Seebeck effect from antiferromagnetic magnons and critical spin fluctuations in epitaxial FeF_2 films. *Phys. Rev. Lett.* **122**, 217204 (2019).

Methods

Characterization of $Cr_2O_3(10\bar{1}0)$ crystal

Cr_2O_3 is a typical uniaxial antiferromagnet with a hexagonal crystal structure and with its magnetic easy axis along the *c* axis (Extended Data Fig. 1a). A Cr_2O_3 $(10\bar{1}0)$ single-crystal slab with an in-plane easy axis (*c* axis) and dimensions of $5 \times 5 \times 1\ mm^3$ was purchased from SurfaceNet GmbH. X-ray diffraction patterns are acquired with an Empyrean X-ray diffractometer with a Cu Kα radiation source. The clear $(30\bar{3}0)$ Bragg peak at a diffraction angle of $2\theta \approx 66°$ (Extended Data Fig. 1b) confirms the $(10\bar{1}0)$ orientation of the crystal. The absence of other peaks over a broad range of 2θ (inset of Extended Data Fig. 1b) suggests the phase purity of the crystal. Tapping-mode atomic force microscopy (Bruker Dimension, Model 5000) characterization (Extended Data Fig. 1c) is performed on the polished surface of the $Cr_2O_3(10\bar{1}0)$crystal. The root-mean-square roughness over a $1\ \mu m \times 1\ \mu m$ area is less than 0.1 nm. A clean and smooth interface is crucial for observing the spin-pumping signal in our experiments.

EMR measurement

Continuous-wave (CW) EMR measurements are performed on a home-built CW EMR spectrometer at the Institute for Terahertz Science and Technology of the University of California, Santa Barbara. A solid-state source, which multiplies the frequency of a 15-GHz synthesizer by a factor of 16 to achieve an output frequency of 0.240 THz, produces a CW power of 55 mW (Virginia Diodes). The incident microwave power is controlled by voltage-controlled attenuation of the source and by a pair of wire-grid polarizers. The sample is secured on a sapphire piece and mounted on a Teflon stage located at the exit of an overmoded waveguide (Thomas Keating). The reflected EMR signal is measured in induction mode, where superheterodyne detection is achieved using a Schottky subharmonic mixer (Virginia Diodes) to mix the 0.240-THz signal down to 10 GHz. A home-made intermediate-frequency stage then amplifies and mixes this 10-GHz signal down to baseband. We modulate the CW source intensity with a frequency of 13.037 Hz, and the reflected signal is measured in quadrature with a pair of lock-in amplifiers (Stanford Research System SR830).

Measurement geometry of AFM spin pumping

In our AFM spin-pumping experiments, the sample is secured on a sapphire piece and mounted on a Teflon stage at the exit of the waveguide. The *c* axis of the Cr_2O_3 $(10\bar{1}0)$ crystal, the propagation direction of 0.240-THz microwaves and the external magnetic fields are all along the same direction.

For electrical detection, we pattern eight Pt strips and eight Ta strips alternately on the polished surface of the Cr_2O_3 $(10\bar{1}0)$ crystal perpendicular to the *c* axis of Cr_2O_3. All parallel strips have the same lateral dimensions of $50\ \mu m \times 3.5$ mm and a thickness of 5 nm. Each of the independent strips produces an EMF like a battery owing to the ISHE during the spin-pumping experiments, but the ISHE voltages from the Pt and Ta strips have opposite polarities owing to their opposite spin Hall angles. To maximize the ISHE signals, we connect these individual 'batteries' in series—that is, positive terminal to negative terminal—to produce a large sum signal. As depicted in Extended Data Fig. 2, we have three detection geometries to probe the ISHE signals, from Pt-only, Ta-only and Pt–Ta hybrid channels. By using multiple strips in each geometry, the ISHE voltage can be effectively multiplied. In addition, a signal preamplifier (SR560) is used to amplify the voltage signals, and the gain is set to 5,000 in all voltage measurements.

SSE measurements

To form the Cr_2O_3/Pt(Ta) heterostructures for the SSE measurements, 5-nm-thick Pt(Ta) is directly deposited on top of the Cr_2O_3 $(10\bar{1}0)$ crystal by magnetron sputtering and patterned into a Hall bar with dimensions of $200\ \mu m \times 2{,}740\ \mu m$ perpendicular to the *c* axis. Then, an 80-nm-thick Al_2O_3 insulating layer is deposited by atomic layer deposition, followed by Cr(45 nm)/Au(5 nm) films covering the Hall bar channel area as a heater. In the SSE experiment, an a.c. current is applied to the Cr/Au heater to generate a vertical temperature gradient across the interface, and the double-frequency voltage response along the Pt(Ta) Hall bar channel is recorded as the spin Seebeck signal V_{SSE} using the standard lock-in technique. The frequency of the a.c. current is set at 13 Hz. An external magnetic field is applied in plane along the easy axis of the Cr_2O_3 (that is, [0001]) or the *c* axis during the SSE measurements. We normalize the SSE voltages by the heating power to draw meaningful comparisons among different measurement conditions.

Data availability

The data that support the plots within this paper and other findings of this study are available from the corresponding author upon reasonable request.

Acknowledgements We acknowledge discussions with S. Zhang, W. Han, I. Barsukov, Y. Liu, T. Su and Y. Liu. Work at University of California Riverside was supported through Spins and Heat in Nanoscale Electronic Systems, an Energy Frontier Research Center funded by the US Department of Energy, Office of Science, Basic Energy Sciences under award number SC0012670 (J.L., M.L., W.Y., M.A. and J.S.). The 0.240-THz measurements were performed at the Institute for Terahertz Science and Technology's (ITST) Terahertz Facilities at the University of California, Santa Barbara, which have been upgraded under NSF award number DMR-1126894. Work by C.B.W., M.K. and M.S.S. was supported by NSF MCB 1617025.

Author contributions J.S. conceived the experiments and supervised the project. J.L. and M.L. fabricated the devices for both the AFMR and SSE experiments with the help of W.Y. and M.A. J.L. and C.B.W. performed the AFMR experiments with the technical assistance of M.K. and N.A., under the supervision of M.S.S. R.C. developed the theoretical model and performed the data analysis with J.L. and P.W. All authors contributed to the writing of the manuscript.

Competing interests The authors declare no competing interests.

Additional information
Supplementary information is available for this paper at https://doi.org/10.1038/s41586-020-1950-4.
Correspondence and requests for materials should be addressed to J.S.
Peer review information *Nature* thanks Chiara Ciccarelli, Aurelien Manchon and the other, anonymous, reviewer(s) for their contribution to the peer review of this work.
Reprints and permissions information is available at http://www.nature.com/reprints.

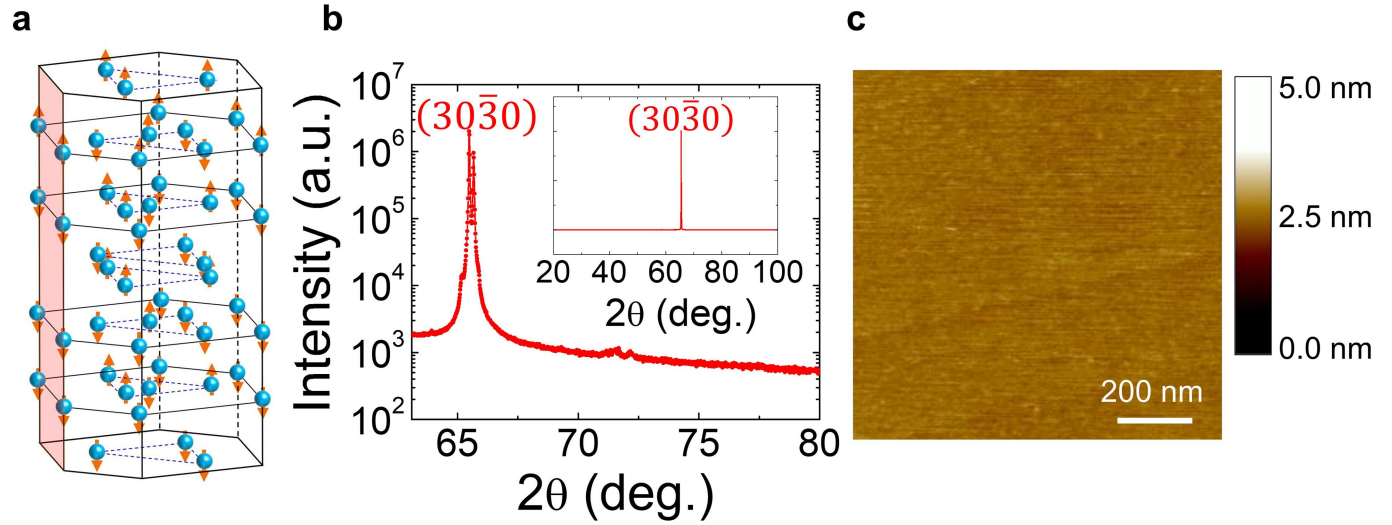

Extended Data Fig. 1 | Crystal structure and surface morphology characterization. a, Crystal structure of Cr_2O_3. The symbols and arrows indicate the Cr atoms and the spins associated with them, respectively. The coloured plane is the $(10\bar{1}0)$ plane. **b**, X-ray diffraction results of the Cr_2O_3 $(10\bar{1}0)$ single crystal. The inset shows the X-ray diffraction results of Cr_2O_3 $(10\bar{1}0)$ over a wide 2θ range. **c**, Atomic-force microscopy image of the polished surface of the Cr_2O_3 $(10\bar{1}0)$ single crystal.

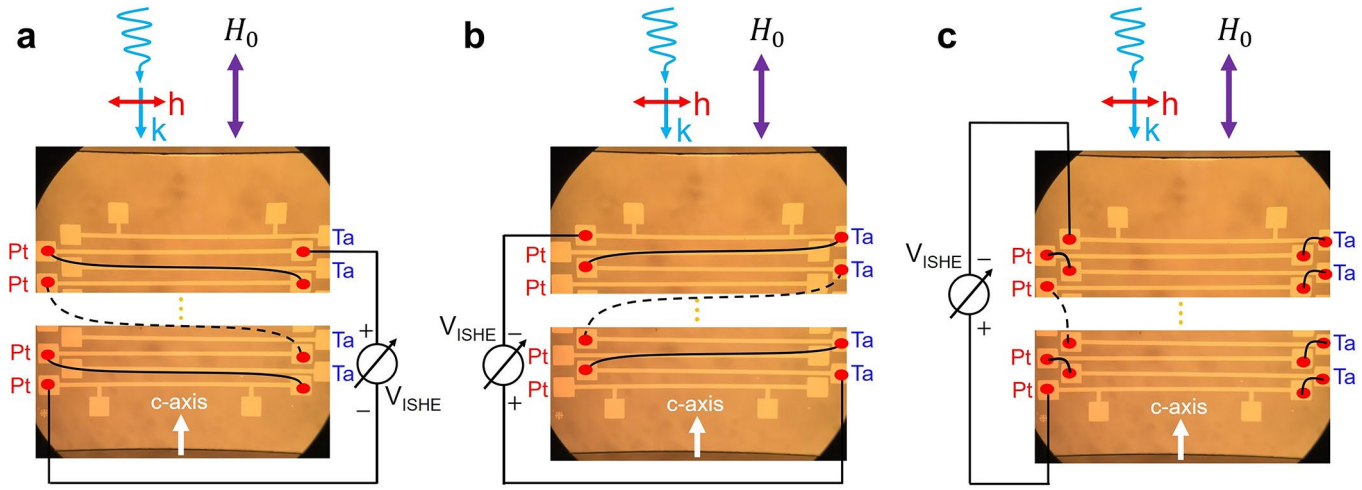

Extended Data Fig. 2 | Measurement geometry of sub-terahertz spin-pumping experiments. a, Pt channel only: only Pt strips are wire-bonded in series. **b**, Ta channel only: only Ta strips are wire-bonded in series. **c**, Pt–Ta hybrid channel. In **a**–**c**, black lines indicate conductive wires that connect the ends of the strips. $\mathbf{H}_0$ is an external magnetic field; **h** and **k** are the magnetic component and wavevector of the 0.240-THz microwaves, respectively. V_{ISHE} is the open-circuit voltage. The white arrows denote the *c* axis of Cr_2O_3 ($10\bar{1}0$).

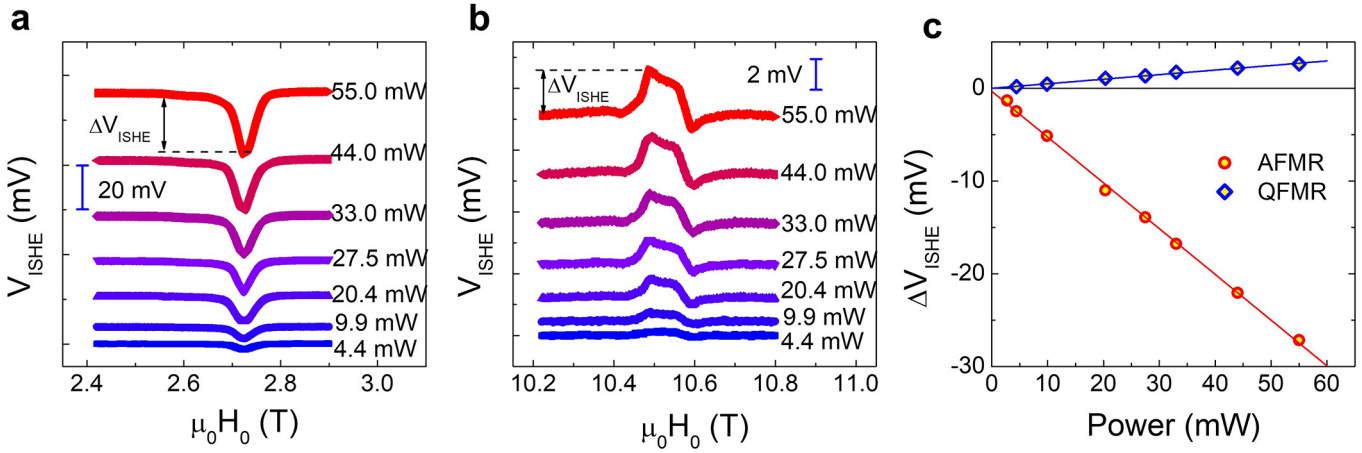

Extended Data Fig. 3 | Linear microwave power dependence of ISHE signals at 10 K. a, Field dependence of the ISHE signal at the AFMR for different microwave powers. **b**, Field dependence of the ISHE signal at the QFMR for different microwave powers. **c**, Microwave power dependence of the ISHE signal magnitude at both the AFMR and the QFMR. ΔV_{ISHE} is defined in **a** and **b**.

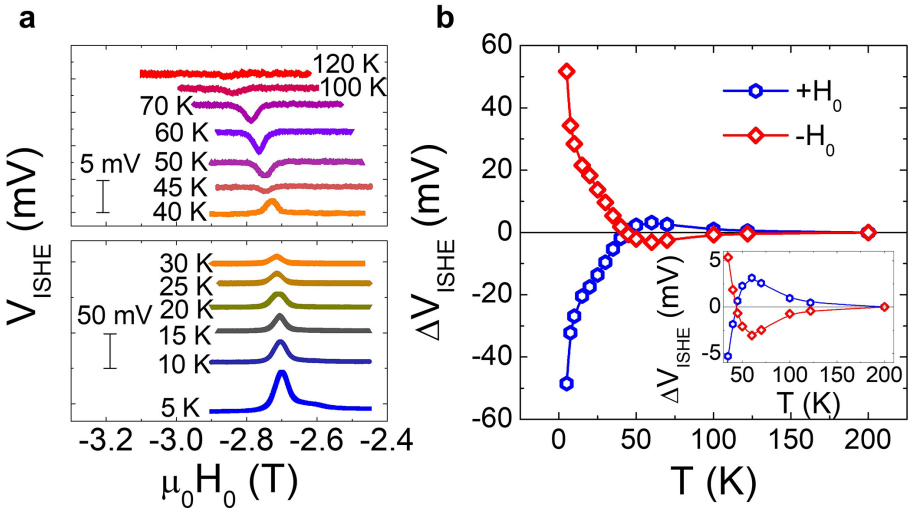

Extended Data Fig. 4 | ISHE signal at the AFMR under negative external magnetic fields H_0. a, ISHE signal as a function of the negative magnetic field $\mathbf{H}_0$ at different temperatures. $\mathbf{H}_0$ is along the easy axis of the Cr_2O_3 $(10\bar{1}0)$ crystal. **b**, Temperature dependence of the magnitude of the ISHE signal under positive and negative magnetic fields. Inset, ISHE signal above 30 K.

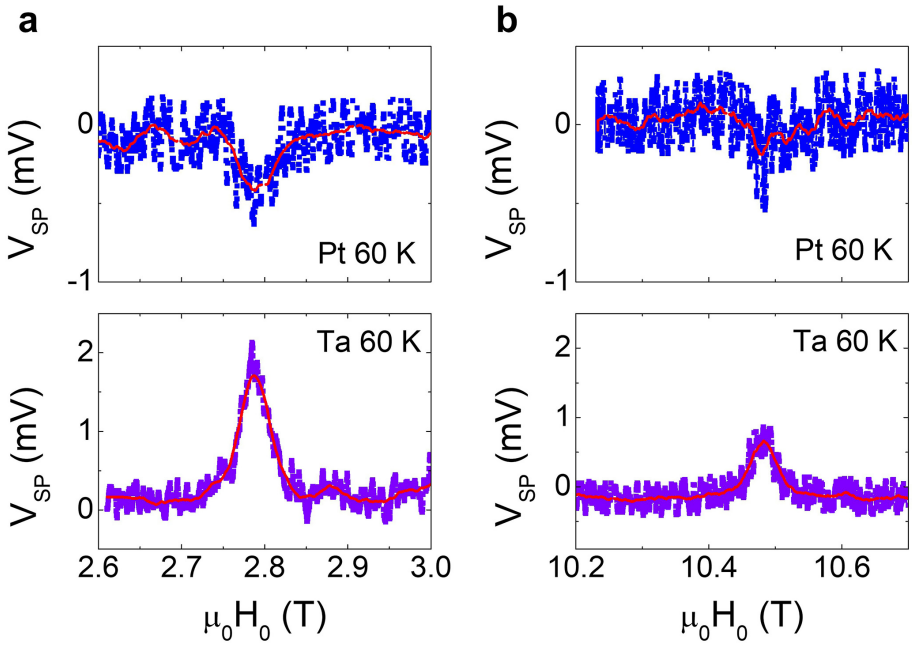

Extended Data Fig. 5 | ISHE signal from Pt- and Ta-only channels at 60 K. **a**, ISHE signal at the AFMR for Pt (top) and Ta (bottom) channels. **b**, ISHE signal at the QFMR for Pt (top) and Ta (bottom) channels. The red curves are smoothed ISHE signals. At the AFMR, the ISHE signals of the Pt and Ta channels at 60 K have opposite signs to that at 5 K (Fig. 2a for Pt and Fig. 2c for Ta). By contrast, the ISHE signal for Pt and Ta at the QFMR maintains the same sign between 60 K and 5 K (Fig. 2b for Pt and Fig. 2d for Ta), which is expected because both coherent and incoherent magnons have the same chirality in the QFMR mode. At and above 60 K, the QFMR voltage signal shows a single Lorentzian peak with a slightly larger linewidth than that of the AFMR peak.

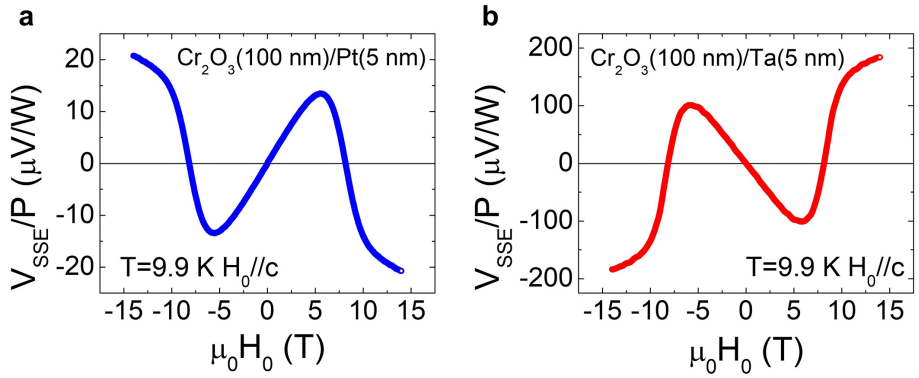

Extended Data Fig. 6 | SSE signal at 9.9 K in Cr_2O_3 (100 nm)/Pt and Cr_2O_3(100 nm)/Ta heterostructures. a, Cr_2O_3 (100 nm)/Pt heterostructure. **b**, Cr_2O_3(100 nm)/Ta heterostructure. The Cr_2O_3 is a $(11\bar{2}0)$-oriented epitaxial thin film deposited on an Al_2O_3 $(11\bar{2}0)$ substrate. The magnetic field is applied along the *c* axis of Cr_2O_3. The SSE signal changes sign across the spin-flop transition, which further confirms that LH magnons (dominating the SSE below the spin-flop transition) and RH magnons (dominating the SSE above the spin-flop transition) carry opposite angular momenta.

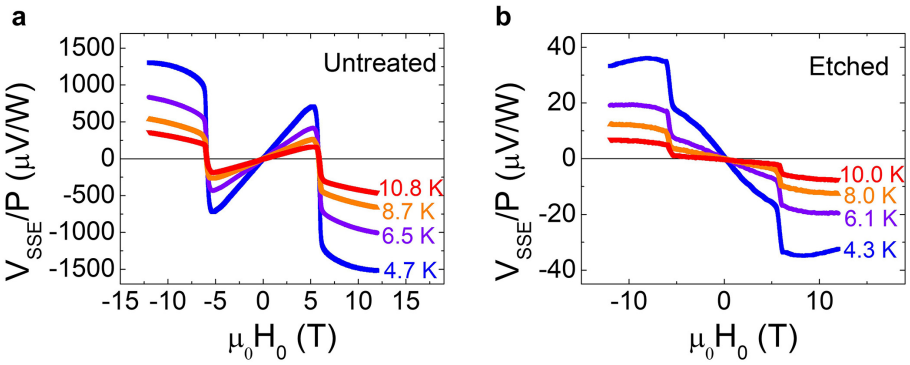

Extended Data Fig. 7 | SSE signal in bulk $Cr_2O_3(10\bar{1}0)$/Pt. a, **b**, Results are shown for bulk $Cr_2O_3(10\bar{1}0)$/Pt with untreated (**a**) and etched (**b**) interfaces. For the untreated sample, we anneal the crystal in air at 600 °C for 2 h using a tube furnace before the deposition of the Pt layer. For the etched sample, we first bombard the surface of the Cr_2O_3 crystal with argon ions using inductively coupled plasma, and then anneal it in air at 600 °C for 2 h using a tube furnace before we deposit the Pt layer. The etching process does not affect the sign of the SSE signal above the spin-flop transition; however, it changes its sign below the spin-flop transition. A possible reason is that the etching process may produce some uncompensated magnetic moments at the interface owing to the different sputtering yields of Cr and O atoms, and these uncompensated magnetic moments also contribute to the SSE signal by modifying the interfacial spin-mixing conductance or directly generating additional spin current. In addition, the etched sample generates a much lower SSE signal than the untreated sample under the same measurement conditions.

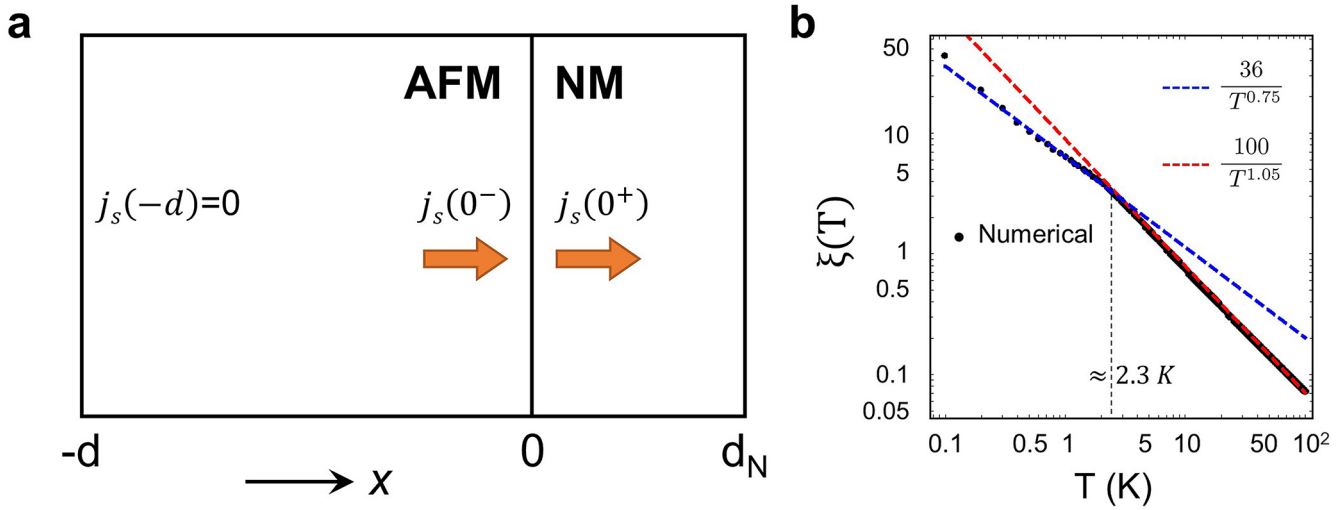

Extended Data Fig. 8 | Schematic illustration of device used for theoretical modelling and numerical results of $\xi(T)$. **a**, Schematic device geometry used to solve the spin diffusion equation of non-equilibrium incoherent magnons (equation (S9) in Supplementary Information). The bilayer structure is represented by an AFM layer and a non-magnetic (NM) metal layer of thickness d and d_N, respectively. **b**, Numerical plot and fittings of $\xi(T)$. Black dots are numerical calculations based on equation (S13) in Supplementary Information. Red and blue dashed lines are power-law fittings for $T > 2.3$ K and $T < 2.3$ K, respectively.